Canadian Fusion Fuels
Technology Project

CFFTP-G--9046

CA9200708

CORROSION OF NICKEL AND STAINLESS STEELS IN CONCENTRATED LITHIUM HYDROXIDE SOLUTIONS

CFFTP G-9046
June 1990

J.W. Graydon* and D.W. Kirk*

CORROSION OF NICKEL AND STAINLESS STEELS IN CONCENTRATED LITHIUM HYDROXIDE SOLUTIONS

CFFTP G-9046
June 1990

J.W. Graydon* and D.W. Kirk*

This is a preprint of a paper submitted to Corrosion.

* Dept. of Chemical Engineering and Applied Chemistry
University of Toronto

ABSTRACT

The corrosion behavior of four alloys in 3 and 5 mol/L lithium hydroxide solutions under a hydrogen atmosphere at 95°C was investigated. Corrosion of Nickel 200 and the stainless steels 316, 316L, and E-Brite® 26-1 was assessed in two sets of immersion tests lasting 10 and 136 days. Corrosion rates were determined by weight loss, susceptibility to stress corrosion cracking was evaluated using U-bends, and the details of the corrosion process were studied on specimens with a mirror finish using light and electron microscopy, x-ray spectrometry and mapping, and x-ray diffraction. The long term corrosion rates were low for all alloys (< 4 μm/y) and no stress corrosion cracking was observed. The corrosion products on the stainless steels were a thin continuous layer of chromium oxide that provided the passivating protection and well-formed crystals that precipitated from solution onto this layer. The crystals were identified as α-$LiFeO_2$, β-$LiFeO_2$, and a very iron-rich β-$LiFe_5O_8$. The passivating layer on the nickel was $Ni(OH)_2$.

The underlying metal corroded evenly except for the 316 stainless steels. These showed a uniform intergranular corrosion with minor drop-out of smaller grains likely because of segregation of impurities to the grain boundaries. The walls of these intergranular crevices were covered with a passivating layer of chromium oxide.

Key Words: lithium hydroxide, stainless steel corrosion, nickel corrosion, intergranular attack.

INTRODUCTION

We have previously investigated the corrosion of carbon steel in concentrated aqueous lithium hydroxide at 95°C under a hydrogen atmosphere as part of a program to examine the possibility of using this solution in a nuclear fusion reactor.[1,2] Although carbon steel is often used to contain concentrated alkali, the corrosion rate was found to be unacceptably high for the present application. Nevertheless, the information about the rates, corrosion products, and corrosion mechanisms that was gathered is a useful guide to understanding the behavior of the more corrosion-resistant, iron-base alloys.

Much improved corrosion performance in hot, strong hydroxide solutions is provided by the chromium-nickel steels and the nickel alloys. There is an extensive body of information on the performance of these alloys in sodium hydroxide since NaOH is a widely used industrial chemical.[3,4] It has been found that, among the stainless steels, type 316 is the alloy of choice for caustic service particularly the low-carbon grade 316L. In certain applications, the high-purity ferritic alloy 26-1 (E-Brite®) has shown superior performance to the conventional stainless steels. Finally, the nickel-base alloys exhibit the best performance particularly pure nickel (Nickel 200), which is resistant even in molten alkali. Although corrosion in alkaline solutions generally depends only on the pH; the corrosion rates, products, and mechanisms of carbon steel in lithium hydroxide have been shown to be different both at 95°C and at 200-316°C.[1] Therefore, it is important to ascertain whether the

performance of the stainless steels and nickel is equally as good in LiOH as in the other hydroxide solutions.

There is little information available about the corrosion of these alloys in aqueous LiOH except for that resulting from the use of LiOH as an anti-corrosion agent in the primary circuit of both boiling and pressurized water reactors to maintain the pH at 10.[5] It has been found that an austenitic stainless is less susceptible to stress corrosion cracking at 360°C in LiOH than in NaOH or KOH solutions although the susceptibility does increase with concentration.[6] The corrosion rate of 304 stainless under a hydrogen atmosphere at 316°C in 2 ppm LiOH was found to be 2 μm/y, while the rate for 347 stainless at 260°C was 0.9 to 1.6 μm/y.[5] There is no information on the corrosion of ferritic stainless nor of nickel in aqueous LiOH. However, Inconel 600® which contains 75% nickel (along with chromium and iron) has been found to corrode in 2.3 ppm LiOH (pH 10) at a rate of 0.46 μm/y at 316°C[7] and, after 1500 hours at 280°C, the LiOH solution contained (in ppb) 1·2 Fe, 1·6 Ni, < 0·1 Cr, and 0·4 Mn.[8] Both the above information on corrosion in high-temperature, very dilute LiOH solutions as well as the extensive data on corrosion in NaOH and KOH solutions indicate the behavior to be expected in concentrated LiOH at temperatures below the boiling point. However, the details of corrosion behavior under these conditions that would occur in the proposed fusion reactor design can only be confidently assessed by direct observation.

The objective of this work was to determine the corrosion rates of 316L, 316, E-Brite 26-1 and Nickel 200 in concentrated lithium hydroxide at 95°C under a hydrogen atmosphere, and to elucidate the corrosion mechanisms by detailed

examination and analysis of the corroded surfaces. The possibility of stress corrosion cracking was also investigated.

EXPERIMENTAL

The composition and mechanical properties of the four alloys tested are listed in Table 1. The procedures for immersion corrosion testing in 3 and 5 mol/L LiOH were adapted from ASTM practice G31-72. The details of this procedure and the methods for assessing corrosion behavior generally followed the process described before.[1] Specimens of a given alloy were suspended on a polypropylene tree in 1L polypropylene bottles and a flow of hydrogen gas through the containers was maintained throughout the test period. Each bottle contained six specimens with a "glass bead" mill finish as well as two specimens with a mirror finish to facilitate study of the detail of the corroded surface. In addition, stress-corrosion cracking was evaluated for each alloy following ASTM practice G30-79. The U-bend specimens were formed from strips measuring 2 x 13 x 127 mm by single-stage bending around a mandrel. This resulted in a 180° bend with a radius of 11 mm and each specimen was secured by an insulated bolt.

Corrosion was assessed after two separate runs, one lasting 10 days and the other lasting 136 days. At the end of each run, the mill-finished specimens were cleaned with 10% nitric acid (stainless steels) or 15% hydrochloric acid (nickel) according to ASTM practice G1-88. In all cases, mechanical removal of corrosion

scale was also required. Since weight losses were quite small, serial weighing during cleaning was essential to obtain reliable measurements of corrosion rates. (G1-88, section 6.1.2)

In addition to the techniques used before for characterization of the corroded surfaces and products of corrosion, elemental analysis by an energy dispersive x-ray spectrometer on the scanning electron microscope was used for both spot analyses and x-ray mapping of the corrosion on the mirror surfaces. The latter permitted a qualitative demonstration of the distribution of elements in the top 1-2 μm of the corrosion scale.

The U-bend specimens were inspected for stress corrosion cracking by examination of both the surface and sections at up to 500x using a light microscope.

RESULTS

Corrosion Rates

The rates for each alloy in both 3 and 5 mol/L solutions were determined after 10 days of corrosion and after 136 days. The numerical results are included in Table 2 and are illustrated graphically in Figure 1. The salient feature of this corrosion data is that very low rates were found for all alloys. There is a decrease in corrosion rate with time, most notably for the E-Brite and Nickel 200. In seven of

the eight pairs there is an increased corrosion rate in the more concentrated hydroxide solution.

The amount of surface scale and the rate of release of oxide into the corroding solution are included in Table 2. The latter quantity has been calculated from specimen weight loss by assuming that the oxide has the same element ratios as the underlying metal, and by using plausible metal oxide/metal ratios (eg Fe_3O_4 / 3Fe = 1·38).[7] In the case of nickel, the corrosion product contains water (as hydroxide). Since the composition is not quite stoichiometric, the values given for oxide release are an upper bound and the actual oxide release is likely close to zero. As calculated, the oxide release rate includes both material lost by dissolution in the LiOH medium as well as loss of solid oxide resulting from sloughing of surface scale.

The much higher amounts of scale found at the longer exposure time indicate that scale thickness increases as corrosion proceeds. In contrast, the release of oxide is much higher at the start of corrosion because of rapid oxidation of unprotected metal and rapid dissolution of oxide into the initially unsaturated solution. Oxides were released more rapidly into the stronger alkaline solution except for E-Brite.

Characterization of the Corrosion Scale

The bulk elemental analysis of the surface scales on the three stainless steels are given in Table 3. The results have been expressed as weight percents of the total cations and, for clarity, the minor elements have been omitted (C, P, S, N,

Cu, Co, Nb). In comparison to the composition of the metal (Table 1) there is generally an enrichment of nickel and iron in the scale, and a depletion of Mn, Cr, and especially Mo. The only exception to these trends is the behavior of Mn in the case of E-Brite where it is somewhat enriched in the scale. The results for 316L and 316 are virtually identical and are mainly independent of hydroxide strength and the duration of corrosion. However the scale on both 316L and 316 in the 5 mol/L solution after 10 days does have relatively higher levels of Cr, Ni and Mo than the other scales. The composition of E-Brite scale is similar under all conditions except that Cr is substantially lower at the longer time in both cases.

Many of the above trends in scale composition are a result of the relative solubilities of the different elements in the LiOH solutions, so the analyses of these solutions after 136 days have been given in Table 4. Only Cr, Mo, and Mn were present above the detection limits (the last in only one case).

Although all specimens were examined microscopically, the mirror surfaces revealed corrosion features more clearly. Corrosion of the mirror surfaces was found to be the same as corrosion of the mill-finish surfaces except as noted below.

After 10 days the only corrosion feature present was very thin, featureless, colorless coatings of corrosion products observed on all specimens.

After 136 days the nickel was coated with a smooth corrosion layer that displayed interference colors. These colors indicated that the corrosion film had a uniform thickness of 200 nm in the 3 mol/L solution and 275 nm in the 5 mol/L. Although the corrosion layer on the mill-finished surfaces was thicker as indicated by

the weight measurements (1160 and 1470 nm respectively), it was also a uniformly thick, smooth coating.

The features found on the 316L and 316 surfaces after 136 days were identical and will be described together. The corroded surfaces appeared uniformly bluish black and displayed three main features under the microscope - an upper layer of octahedral crystals, a thin base layer that coated the metal, and deep intergranular crevices (Figure 2).

The surface was covered with a mixture of well-formed, opaque, octahedral crystals 2-3 μm in size (Figure 3) and smaller, less well-formed, red-brown octahedral crystals. The latter were situated on top of the larger crystals (Figure 4) and their abundance was variable from specimen to specimen. In some areas both types of crystal formed a continuous layer, in other areas they covered only part of the surface, and in some places they had sloughed off either individually or *en masse* (e.g. Figure 2). Although strongly attached, some isolated crystals could be removed mechanically without breaking. A typical semi-quantitative analysis of a large, opaque crystal by x-ray spectrometer is listed in Table 5. Oxygen and lithium were not measured due to the low energy of their x-rays and low levels of manganese could not be detected since its x-ray peak was superimposed on the chromium Kβ peak. The analysis reveals an enrichment of Fe Ni and Si and a marked depletion of Cr compared to the composition of the underlying alloy.

The base layer (Figure 5) was a featureless transparent coating displaying interference colors that indicated its thickness was about 170 nm. Although this layer did extend beneath the crystals, it was somewhat thinner there (80 nm). The

uppermost part of this layer bridges the intergranular crevices in places where it has not yet been fragmented (Figure 6). Although too thin for quantitative microanalysis, an x-ray map (Figure 7) shows that this layer is composed mainly of chromium. Since the layer is thin, there are a number of x-rays originating from the underlying metal and thus iron and nickel also show. The fact that the crevice is manifest in the iron and nickel maps by fewer spots while the chromium shows no similar decrease indicates that the chromium base layer extends down into the crevice, lining the side walls.

The corrosion crevices are entirely intergranular with a remarkably uniform width of 1.4 μm at the surface and extend to a depth of about 4 μm, gradually tapering inward (Figures 2, 5). This corrosion was enough to undermine a few of the smaller metal grains which then dropped out. No other type of selective corrosion such as pitting is evident.

The E-Brite was partially covered with patches of corrosion product that appeared blue-black on specimens from the 3 mol/L solution and dark brown on those from the more concentrated solution. Microscopically, these patches consisted of small, well-formed crystals that were red-brown, transparent cubo-octahedra in the 5 mol/L solution (Figure 8) and were black, nearly opaque octahedra in the 3 mol/L solution. Also, there was a thin, slightly brown, uniform coating that covered the entire surface of the metal between the crystals (the cracks are artefacts resulting from drying). X-ray mapping showed that this layer consisted mainly of chromium. There was no evidence of intergranular corrosion or any other type of selective attack.

Both reflection and powder x-ray diffraction were used to identify the phases present in the corrosion products. The former also gave information on any preferred crystallographic orientation of these phases.

The coating on Nickel 200 was found to be hexagonal $Ni(OH)_2$ that was strongly oriented with the c axis perpendicular to the metal surface. No lines for any lithium-nickel compounds were present.

The corrosion products on 316L and 316 from both solution concentrations all gave identical reflection patterns. These patterns indicated the presence of the same two phases as were observed before in the corrosion of carbon steel.[1] Of the 11 lines present, 9 were from a disordered, very iron-rich spinel β-$LiFe_5O_8$ and 4 were from a disordered, somewhat iron-rich α-$LiFeO_2$ which has a rock-salt structure. Three lines were superimposed lines from both phases and one was not identified. The relative line intensities indicated that there was some preferential orientation of the fcc spinel with (1,1,1) planes perpendicular to the metal surface, and that the relative amounts of the two phases varied from 10 to 20% $LiFeO_2$ and 80 to 90% $LiFe_5O_8$. Significantly, there were no lines for the phase that makes up the chromium-rich base layer.

Both reflection and powder patterns were obtained for the corrosion products on the E-Brite. Two phases were present in varying amounts. The predominant phase in the 5 mol/L solution was stoichiometric α-$LiFeO_2$, the same disordered cubic phase that was present on the 316 steels. The predominant phase in the 3 mol/L solution was β-$LiFeO_2$, an ordered tetragonal polymorph. As with the other stainless steels, the chromium base layer produced no lines.

Careful microscopic examination of U-bend specimens made from each alloy both on the surface and in section revealed no stress corrosion cracking. Surprisingly, in the case of the 316L and 316 steels, there was none of the intergranular attack that was observed in the unstressed specimens. In all cases, there were no corrosion products present on the surface except for a transparent, smooth coating. The thickness of this coating as revealed by the interference colors was different for each type of alloy.

DISCUSSION

The corrosion rates for all four alloys in both concentrations of LiOH were found to be below 4 μm/y during the long term test and thus the alloys appear quite suitable for application in a nuclear fusion reactor. Despite the somewhat different properties of lithium compared to the other alkali metals, these corrosion rates are similar to those observed for these alloys in NaOH under similar conditions.[3,4] Since the corrosion rates of these alloys in alkali are determined by the amount of protection afforded by the surface corrosion scale, it is clear that the component of the scale that provides protection for each alloy must be the same for LiOH as for the other hydroxides. In particular, since the iron corrosion products are different in LiOH solutions and it is known that they result in higher corrosion rates when they are the only protection (as on carbon steel),[1] the $LiFe_5O_8$ and $LiFeO_2$ crystals can have no effect on the corrosion rates of stainless steels in LiOH.

When any of the alloys is first immersed in hydroxide, there is an initial, rapid attack of the metal until the corrosion-resistant layer is built up. That is, the surface oxide formed in the atmosphere is inadequate for protection from hot, concentrated LiOH. Once established, however, the resistant layer provides excellent protection and the corrosion rates drop, dramatically so in the case of E-Brite and Nickel 200. This decrease in corrosion rates is paralleled by even more marked drops in the rates of oxide release into the solution, so that the amount of surface scale increases (Table 2).

The increase in the corrosion rate that was found in the more concentrated LiOH solution in all but one case averaged 34%. This is the same as the increase in the concentration of hydroxyl ions in the 5 mol/L LiOH solution (33%) indicating that the corrosion rate is proportional to the concentration of dissociated hydroxide, at least in concentrated solutions. This relationship does not appear to hold for E-Brite at the longer corrosion time possibly because of a change in the character of the film formed in 5 mol/L LiOH that affords greater protection. The details of the corrosion process that occurs on each type of alloy will be discussed separately.

Nickel 200

The corrosion of commercially pure nickel, Nickel 200, is the simplest. Nickel is oxidized to the hydroxide which is then deposited from solution onto the surface of the metal in a continuous, even film composed of highly-oriented hexagonal crystals that provide excellent protection from corrosion. As with all alloys studied, the oxidant is water (1).

$$Ni + 2H_2O \rightarrow Ni(OH)_2 + H_2 \qquad (1)$$

The crystal size which, from the sharpness of the diffraction lines, is greater than 0.2 μm indicates that the hydroxide is deposited from solution rather than formed directly at the metal surface. Direct formation of hydroxide at the metal surface would normally produce much smaller crystals at 95°C. The solubility of nickel in both hydroxide solutions is very low (<0.1 ppm) and the growth of $Ni(OH)_2$ is sufficiently fast that supersaturation does not occur in the bulk of the solution (Table 4). There is evidence that the $Ni(OH)_2$ may be somewhat deficient in water since the weight of the scale is somewhat less than is expected based on the amount of metal oxidized. Despite the inherent reactivity of nickel with concentrated hydroxide as evidenced by the high initial corrosion rates, the tenacious impervious nature of the coating and its low solubility give nickel the best performance of the alloys studied not only in LiOH but also in all other alkalies (except ammonium).[3]

316L and 316

Both austenitic steels had identical corrosion rates and products. The corrosion resistance is provided by the thin, continuous, chromium-rich layer that is almost certainly Cr_2O_3. The complete absence of any lines from this phase in the diffraction pattern indicates a very small crystal size (likely < 10 nm) which is characteristic of oxide films formed directly by oxidation *in situ* rather than deposited from solution. The corrosion film at ten days formed a continuous coating on the metal and, even at 136 days, there are remnants of this initial layer bridging the

crevices (Figure 6). However, some time after 10 days of corrosion, the coating loses its protective ability at the grain boundaries leading to the formation of uniform intergranular crevices.

One very common cause of intergranular attack in austenitic steels is heat sensitization that produces a depletion of chromium near the grain boundaries. This low chromium content causes a much greater susceptibility to corrosion that results in severe selective dissolution of metal at the grain boundaries. The possibility that heat sensitization existed in the 316L and 316 specimens was investigated by using the recommended electrolytic, oxalic acid etching procedure for detecting this condition (ASTM practice A262-86). The resulting step structure with a total absence of any ditches at grain boundaries indicated that no chromium depletion was present at the grain boundaries.

The other cause of selective corrosion at grain boundaries in alloy steels results from the segregation of certain components to the edge of the grains. In particular, it has been shown that the concentration of phosphorus and silicon in austenitic stainless steels is elevated near grain boundaries, and that this can lead to intergranular attack and increased corrosion rates.[9,10] Similarly, in low alloy steels phosphorus and, to a lesser extent, molybdenum segregation to grain boundaries significantly impaired the caustic cracking resistance.[11] The precise mechanism by which the segregated elements enhance corrosion is not known. However, at least in LiOH, the chromium film that initially forms over grain boundaries is not ultimately protective because of mechanical or atomic defects, and the hydroxide rapidly attacks the intergranular plane. The remarkable uniformity of the width of the

crevices thus created and the layer of passivating chromium demonstrated on the walls of the crevice indicate that the walls, once exposed, develop the same protective layer and corrode at the same uniform rate as the surface. That is, the susceptibility to corrosion is the result of impurities at the grain boundary only and the resistance of the near-boundary portion of the grain serves to mitigate the effects of this selective attack thus slowing the penetration and subsequent drop-out of grains.

Although the coating of Cr_2O_3 is responsible for the corrosion resistance of these steels, it is not the major component of the corrosion scale. Most of the iron, nickel and silicon that are corroded from the alloy enter the LiOH solution and are then precipitated on top of the Cr_2O_3 layer as a mixture of two types of well-formed octahedral crystals. These crystals are primarily lithium-iron oxides, one with a rock-salt structure - $LiFeO_2$, and the other with a spinel structure - $LiFe_5O_8$. Despite the admixture of Ni, Si and minor Cr in their structures, their x-ray diffraction patterns are identical with those of the crystals formed during the corrosion of carbon steel under the same conditions, and both the reactions that result in their formation and the details of their structure have been discussed before.[1] It is significant that, despite the much lower corrosion rate of stainless and hence the slower release of iron into solution, the structures and relative abundance of both phases are the same. Although not evident in the bulk of the solution, the degree of supersaturation of iron near the surface of the corroding stainless must be similar to that near the carbon steel. This supersaturation results in the enrichment of iron beyond the stoichiometric amount in both phases.

The overall composition of the scales is determined by the solubility of the alloy components in the LiOH solutions, which have hydroxide ion concentrations of 0.43 and 0.57 mol/L.[1] Based on their solubility products in the presence of hydrogen; Fe, Mn, and Ni all have solubilities below 200 ppb while Cr has a solubility of about 5 ppm and Si and Mo are both very soluble. Thus, Mo is very depleted in the scale relative to the underlying alloy, and Cr is somewhat depleted. (Not all of the Cr depletion can be explained by the dissolution of Cr in LiOH and is partly due to the difficulty in cleaning all of the chromium-rich scale from the metal surface and crevices for analysis.) Since Mn is a minor component of the alloy, a substantial fraction of the Mn that is oxidized remains dissolved in the solution despite its limited solubility and is thus depleted in the scale. In contrast, both Ni and Fe reach their solubility limits early and are almost entirely deposited in the scale. The behaviour of Si is somewhat anomalous in that it is slightly enriched in the scale despite its high solubility. The relatively iron-poor scale in 5 mol/L LiOH after 10 days may be the result of iron supersaturation in this solution. Thus, at 10 days a significant fraction of all of the iron oxidized is held in solution. In all cases at 136 days, the LiOH solutions are saturated with all of the major alloy elements except Si and Mo.

E-Brite 26-1

E-Brite is a ferritic stainless with very low levels of the interstitials C and N, and these levels are further lowered by the addition of Nb. It has high levels of Cr and Mo and exhibits superior resistance to many types of localized corrosion (pitting,

stress corrosion cracking, intergranular attack).[3] Its corrosion behaviour in LiOH differs in many respects from that of austenitic stainless. Although the initial corrosion rates are quite high, its long term corrosion rates are substantially better than the 316 stainless and approach those for nickel. Also, the oxide release rate is lower in the 5 mol/L solution than the 3 resulting in a lower long-term corrosion rate in the more concentrated solution. However, the most striking difference in behaviour is the complete immunity of this alloy from intergranular corrosion and subsequent drop-out of grains. This freedom from attack at the grain boundaries may be due to the lower levels of P, Si or Mo in the alloy, and is primarily responsible for the lower corrosion rates compared to 316L and 316. The lower corrosion rate in turn decreases the rate of iron precipitation from solution. This not only favors the formation of the low-iron lithium oxide $LiFeO_2$, but also this phase is stoichiometric according to its cell constant rather than iron-rich as in the case of the crystals on the austenitic alloys. The relative abundance of the brown α and the black β polymorphs of $LiFeO_2$ is controlled by LiOH concentration with the lower concentration favoring the latter structure. This latter phase is not seen at all in the scale on the 316 alloys.

The protective chromium-rich coating is considerably smoother and thinner than that on the 316 alloys (< 80 nm from the interference colors). The very low chromium levels in the bulk scale analysis, particularly after the longer corrosion time, are a reflection of the thinness of this coating. The lower corrosion rates are partly due to the superior protection that this Cr_2O_3 film provides compared to that on the 316 alloys. The better quality of this film is likely because of the higher

chromium content of the underlying alloy that produces a more compact, impervious coating.

The complete absence of stress corrosion cracking in the U-bends is encouraging since caustic cracking can be a major problem at higher temperatures. Although there are additional factors such as the effect of fluid flow, heat flux and neutron flux that may influence the corrosion behaviour of these alloys, the corrosion information that has been presented indicates the basic compatibility of all alloys tested with hot, concentrated lithium hydroxide.

CONCLUSIONS

1. All alloys tested possess sufficient immunity to concentrated LiOH at 95°C under a hydrogen atmosphere to contain this solution for use as a breeding blanket in a nuclear fusion reactor.

2. The austenitic stainless steels are subject to mild intergranular corrosion and grain drop-out but show no evidence of stress corrosion cracking. E-Brite 26-1 and Nickel 200 provide the lowest corrosion rates and show no localized corrosion.

3. The structure of the coating that provided protection was crystalline $Ni(OH)_2$ on the nickel and a non-crystalline Cr_2O_3 on the stainless steels. The iron, nickel, and silicon produced by oxidation of the stainless steels were deposited from solution as well-formed crystals of various lithium-iron oxide phases.

4. The bulk elemental composition of the corrosion scales is primarily determined by the solubility of the individual components in the hydroxide solutions.

ACKNOWLEDGEMENTS

The authors gratefully acknowledge the financial and technical support provided by the Canadian Fusion Fuels Technology Program (CFFTP) for this work.

REFERENCES

1. J.W. Graydon and D.W. Kirk, Corrosion, to be published (1990).
2. D. Steiner, M. Embrechts, G. Versamis, K. Wrisley, L. Deutsch, and P. Gierzewski, Fusion Technology 10 (1986): p. 641.
3. J.K. Nelson, "Metals Handbook Vol. 13 (Corrosion)" (Metals Park, OH: ASM International, 1987), pp. 547, 643.
4. D. Behreus, "Dechema Corrosion Handbook Vol. 2" (New York, NY: VCH Publishers, 1988), p. 83.
5. D. Behreus, "Dechema Corrosion Handbook Vol. 3" (New York, NY: VCH Publishers, 1988), p. 219.
6. H. Coriou, L. Grall and M. Pelras, Energ. Nucl. 9 (1967): p. 303; (in Chem. Abs. 68-15504).
7. D. van Royen, H.R. Copson and W.E. Berry, Corrosion 25 (1969): p. 194.
8. C.F. Cheng, Corrosion 20 (1964): p. 341t.
9. R.L. Cowan II and C.S. Tedmon Jr. Advan. in Corros. Sci. and Technol. 3 (1973): p. 345.
10. A.J. Jacobs, Corrosion 46 (1990): p. 30.
11. N. Bandyopadhyay and C.L. Briant, Corrosion 41 (1985): p. 274.

TABLE 1. Chemical Analysis and Mechanical Properties of Alloys

Alloy	Mechanical Properties (MPa)		Chemical Composition (wt%)								
	Yield Strength	Tensile Strength	C	Mn	P	S	Si	Cr	Ni	Mo	Other
316 Stainless	276	604	0.052	1.44	0.022	0.008	0.42	16.74	10.07	2.06	Cu 0.11 N 0.057 Co 0.21
316L Stainless	270	587	0.021	1.04	0.028	0.004	0.64	16.92	11.31	2.05	N 0.048
Nickel 200	-	-	0.08	0.23	-	0.001	0.02	-	bal	-	Fe 0.01
E-Brite 26-1	390	534	0.009	0.040	0.012	-	0.18	26.33	0.13	1.00	Cu 0.01 Nb 0.11 N 0.0091

TABLE 2. Corrosion Rates and Scale Production

Alloy	LiOH Solution Concentration (mol/L)	Exposure Time (days)	Corrosion Rate(μm/y)*	Scale (mg/cm^2)	Oxide Release Rate ($mg/cm^2.y$)
316L	3	10	2.87 ± 0.23	0.05	1.28 ± 0.36
		136	2.42 ± 0.16	0.84	0.44 ± 0.11
	5	10	4.97 ± 0.88	0.09	2.26 ± 0.49
		136	3.47 ± 0.60	1.04	1.05 ± 0.24
316	3	10	3.67 ± 0.46	0.07	1.39 ± 0.40
		136	2.59 ± 0.18	0.89	0.48 ± 0.13
	5	10	4.82 ± 0.57	0.07	2.81 ± 0.57
		136	3.37 ± 0.35	0.95	1.19 ± 0.32
E-Brite	3	10	5.23 ± 1.00	0.04	4.38 ± 1.29
		136	1.82 ± 0.09	0.60	0.43 ± 0.22
	5	10	6.14 ± 0.42	0.14	1.32 ± 0.51
		136	1.58 ± 0.07	0.52	0.37 ± 0.13
Nickel 200	3	10	5.89 ± 0.78	0.11	-
		136	1.07 ± 0.21	0.48	<0.26
	5	10	6.30 ± 1.26	0.19	-
		136	1.26 ± 0.16	0.61	<0.22

* average and standard deviation of six specimens

TABLE 3. Elemental Analysis of Corrosion Scale

Alloy	Solution Concentration (mol/L)	Exposure Time (days)	Element (wt%)*					
			Fe	Mn	Si**	Cr	Ni	Mo
316L	3	10	73	0.70	0.60	6.4	18.0	0.20
		134	74	0.81	0.98	6.6	18.5	0.13
	5	10	69	0.76	-	9.3	28.0	0.32
		134	73	0.63	-	7.3	18.9	0.13
316	3	10	76	0.85	0.82	5.5	15.4	0.19
		134	74	0.98	-	6.8	18.2	0.15
	5	10	67	1.00	-	8.0	22.3	0.23
		134	75	0.81	-	6.6	17.8	0.15
E-Brite	3	10	89	0.13	0.20	8.3	0.73	<0.01
		134	94	0.15	-	3.8	0.90	0.07
	5	10	88	0.09	-	9.7	0.88	0.05
		134	96	0.12	-	2.4	0.74	0.04

* excluding oxygen, hydrogen and lithium

** some samples were not analysed for Si

TABLE 4. Elemental Analysis of Corroding Solutions after 136 days

Alloy	Solution Concentration (mol/L)	Element (mg/L) Fe	Mn	Cr	Ni	Mo
316L	3M	<5	<0.2	9.8	<0.1	2.6
	5M	<5	<0.2	12.1	<0.1	4.2
316	3M	<5	0.2	10.9	<0.1	3.5
	5M	<5	<0.2	12.8	<0.1	4.4
E-Brite	3M	<5	<0.1	10.5	<0.1	1.0
	5M	<5	0.2	5.1	<0.1	0.6
Nickel	3M	<5	<0.2	<0.2	<0.1	<0.1
	5M	<5	<0.1	<0.2	<0.1	<0.1

TABLE 5. Elemental Analysis of Large Opaque Crystal on 316L at 136 days by X-ray Spectrometer

Element	Weight %
Si	1.0
Cr	4.3
Fe	80.7
Ni	13.9

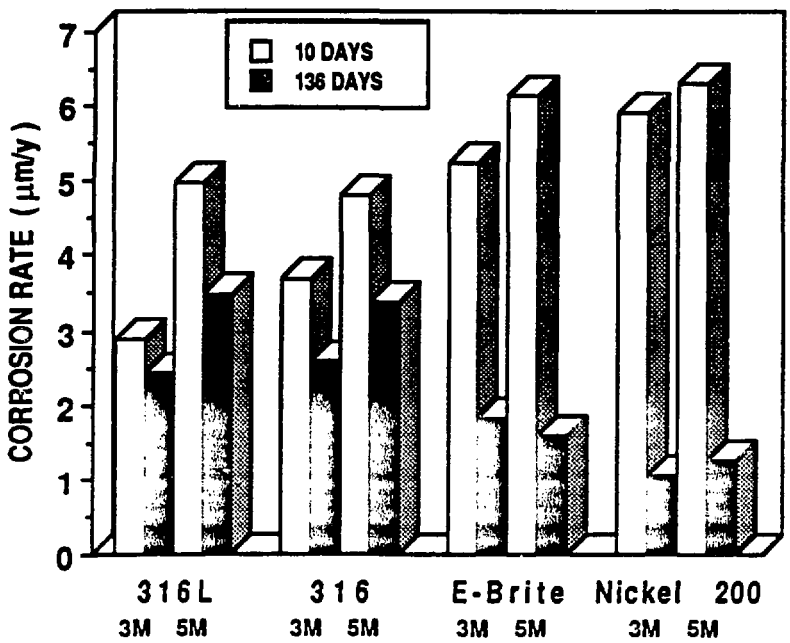

Figure 1. Corrosion rates of the four alloys in aqueous solutions of LiOH at 95°C under a hydrogen atmosphere. The effect of solution concentration (3 and 5 mol/L) and duration of corrosion (10 and 136 days) are shown.

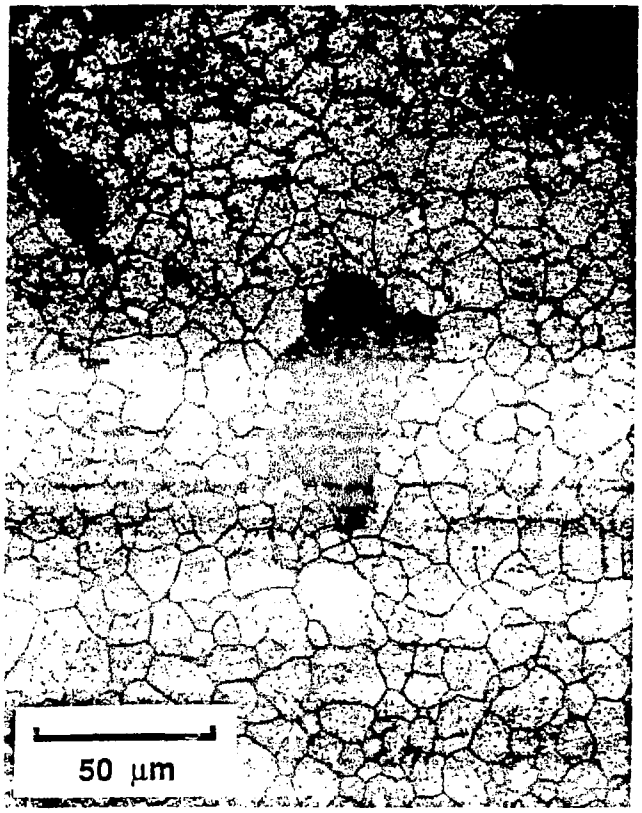

Figure 2. Light photomicrograph of the surface of 316 stainless after 136 days in 5 mol/L LiOH showing uniform intergranular attack, scattered grain drop-out, and the mottled base layer of Cr_2O_3. The dark gray patches are lithium-iron oxide crystals that have not yet sloughed off.

Figure 3. Scanning electron micrograph of optically opaque octahedral crystals of the spinel $LiFe_5O_8$ on the surface of the same specimen as in Figure 2.

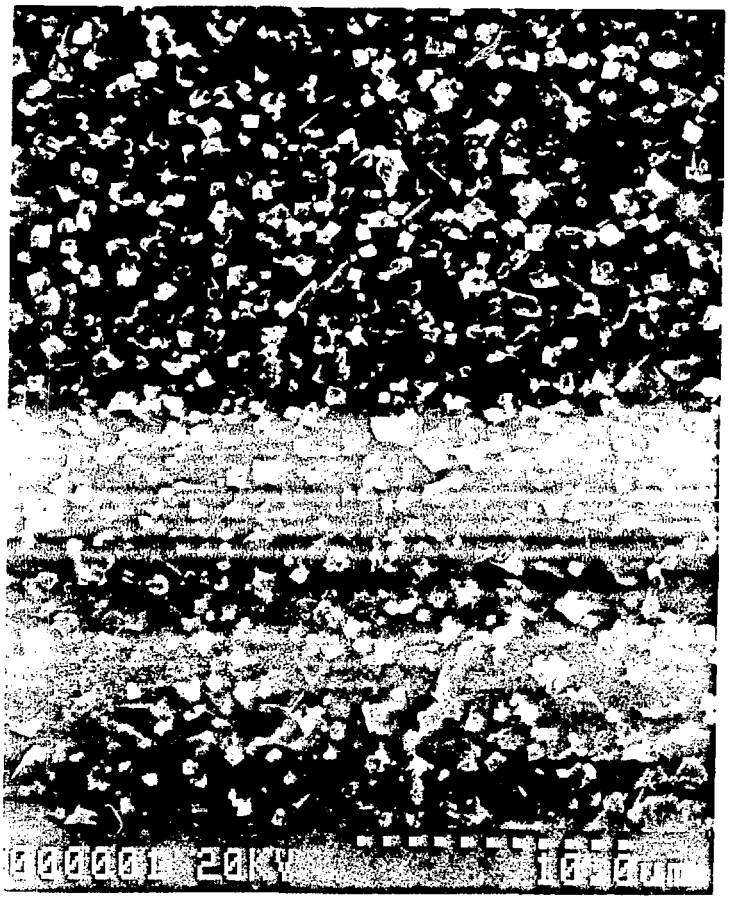

Figure 4. Surface of 316L stainless in 3 mol/L LiOH showing small, poorly-formed crystals of $LiFeO_2$ (white) with larger, well-formed octahedra of $LiFe_5O_8$ beneath (dark grey).

Figure 5. Surface of same specimen as in Figure 2 showing the character of the Cr_2O_3 base layer, the uniform intergranular attack, and the depression where a grain has dropped out (lower right).

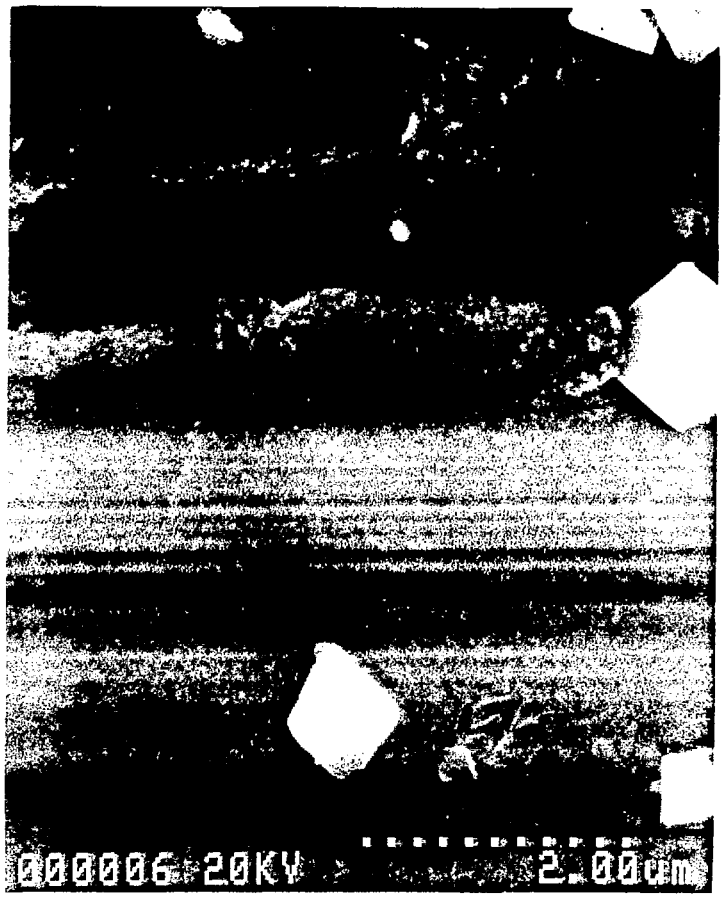

Figure 6. Detail of the surface of 316L in 5 mol/L showing a thin film of the base layer bridging the intergranular crevice at upper right. Also visible are the "scars" in this base layer where the octahedral crystals have sloughed off (upper left).

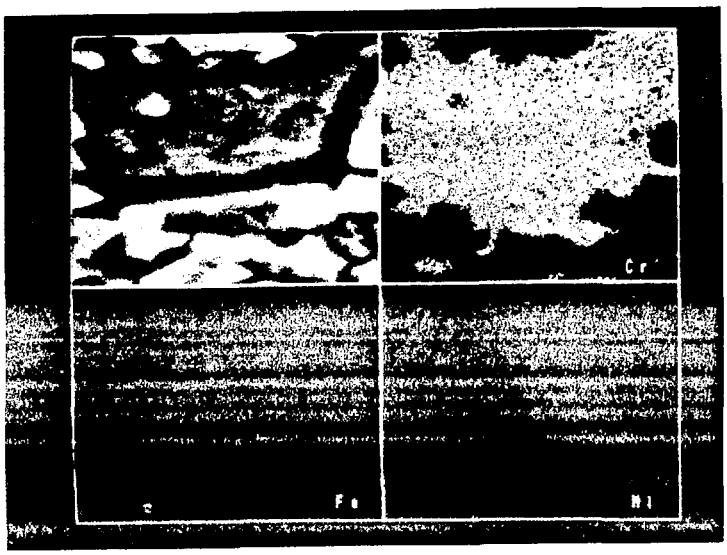

Figure 7. Scanning electron micrograph and elemental x-ray maps of an area similar to that in Figure 6 showing surface distribution of chromium, iron, and nickel. Chromium is absent from the crystals but is abundant in the base oxide which extends down into the intergranular crevice. Iron and nickel are abundant both in the crystals and the underlying metal but are decreased in the crevice.

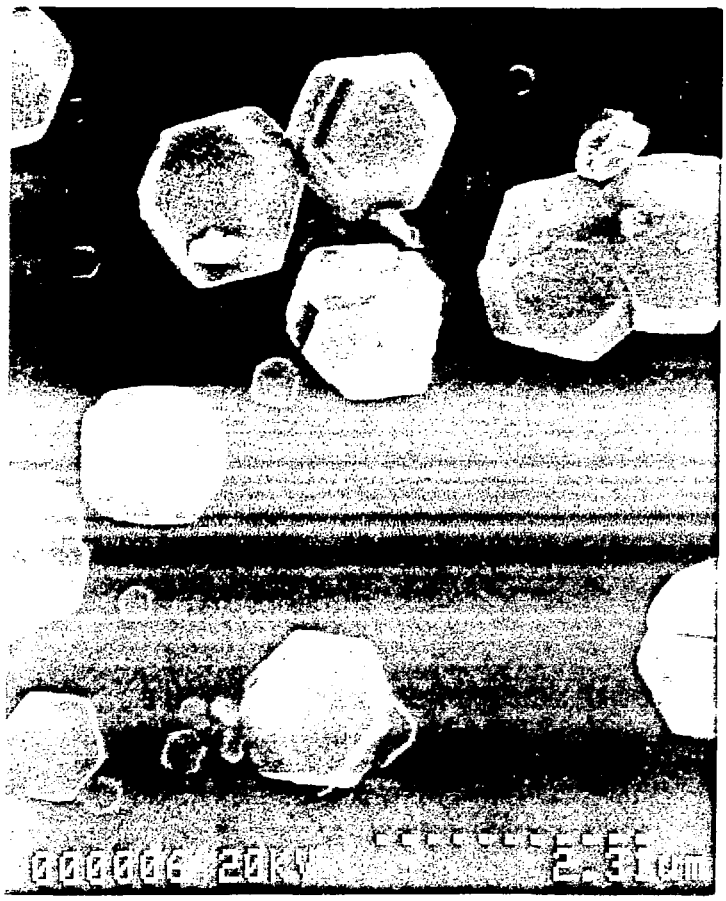

Figure 8. Surface of E-Brite in 5 mol/L showing well-formed cubo-octahedra of $LiFeO_2$ and a crack in the smooth, underlying coating.